Interferometric second harmonic generation microscopy

Siavash Yazdanfar, Lily H. Laiho, Peter T. C. So

Department of Mechanical Engineering and Division of Biological Engineering
Massachusetts Institute of Technology, Cambridge, MA 02139
siavash@mit.edu, ptso@mit.edu

Abstract: We describe a novel second harmonic generation (SHG) microscope that employs heterodyne detection by interfering the epidirected SHG from a sample with SHG from a reference crystal. In addition, the microscope provides complementary reflectance information based on optical coherence microscopy (OCM). The instrument features dual balanced detection to minimize the effect of source fluctuations, and polarization-sensitive detection to measure the nonlinear susceptibility of the sample. Interferometric detection can potentially improve the sensitivity and thus extend the imaging depth as compared with direct detection of SHG.

OCIS codes: (190.4160) Multiharmonic generation; (170.4500) Optical coherence tomography; (180.6900) Three-dimensional microscopy; (170.0110) Imaging systems

---

References and links

1. Y. R. Shen, "Surface properties probed by second-harmonic and sum-frequency generation," Nature **337**, 519-525 (1989).
2. R. M. Corn and D. A. Higgins, "Optical second harmonic generation as a probe of surface chemistry," Chem. Rev. **94**, 107-125 (1994).
3. Y. Guo, P. P. Ho, H. Savage, D. Harris, P. Sacks, S. Schantz, F. Liu, N. Zhadin and R. R. Alfano, "Second-harmonic tomography of tissues," Opt. Lett. **22**, 1323-1325 (1997).
4. P. J. Campagnola, M.-D. Wei, A. Lewis and L. M. Loew, "High-resolution nonlinear optical imaging of live cells by second harmonic generation," Biophys. J. **77**, 3341-3349 (1999).
5. L. Moreaux, O. Sandre, M. Blanchard-Desce and J. Mertz, "Membrane imaging by simultaneous second-harmonic generation and two-photon microscopy," Opt. Lett. **25**, 320-322 (2000).
6. A. Zoumi, A. Yeh and B. J. Tromberg, "Imaging cells and extracellular matrix in vivo by using second-harmonic generation and two-photon excited fluorescence," Proc. Nat. Acad. Sci. USA **99**, 11014-11019 (2002).
7. W. R. Zipfel, R. M. Williams, R. Christie, A. Y. Nikitin, B. T. Hyman and W. W. Webb, "Live tissue intrinsic emission microscopy using multiphoton-excited native fluorescence and second harmonic generation," Proc. Nat. Acad. Sci. USA **100**, 7075-7080 (2003).
8. R. K. Chang, J. Ducuing and N. Bloembergen, "Relative phase measurement between fundamental and second-harmonic light," Phys. Rev. Lett. **15**, 6-8 (1965).
9. K. Kemnitz, K. Bhattacharyya, J. M. Hicks, G. R. Pinto and K. B. Eisenthal, "The phase of second-harmonic light generated at an interface and its relation to absolute molecular orientation," Chem. Phys. Lett. **131**, 285-290 (1986).
10. R. Stolle, G. Marowsky, E. Schwarzberg and G. Berkovic, "Phase measurements in nonlinear optics," Appl. Phys. B **63**, 491-498 (1996).
11. J. Chen, S. Machida and Y. Yamanoto, "Simultaneous measurement of amplitude and phase in surface second-harmonic generation," Opt. Lett. **23**, 676-678 (1998).
12. D. Huang, E. A. Swanson, C. P. Lin, J. S. Schuman, W. G. Stinson, W. Chang, M. R. Hee, T. Flotte, K. Gregory, C. A. Puliafito and J. G. Fujimoto, "Optical coherence tomography," Science **254**, 1178-1181 (1991).
13. P. T. C. So, C. Y. Dong, B. R. Masters and K. M. Berland, "Two-photon excitation fluorescence microscopy," Annu. Rev. Biomed. Eng. **2**, 399-429 (2000).
14. J. A. Izatt, M. R. Hee, G. M. Owen, E. A. Swanson and J. G. Fujimoto, "Optical coherence microscopy in scattering media," Opt. Lett. **19**, 590-592 (1994).

15. A. M. Rollins and J. A. Izatt, "Optimal interferometer designs for optical coherence tomography," Opt. Lett. **24**, 1484-1486 (1999).
16. B. M. Hoeling, A. D. Fernandez, R. C. Haskell, E. Huang, W. R. Myers, D. C. Petersen, S. E. Ungersma, R. Wang, M. E. Williams and S. E. Fraser, "An optical coherence microscope for 3-dimensional imaging in developmental biology," Opt. Express **6**, 136-146 (2000).
http://www.opticsexpress.org/abstract.cfm?URI=OPEX-6-7-136
17. A. D. Aguirre, P. Hsiung, T. H. Ko, I. Hartl and J. G. Fujimoto, "High-resolution optical coherence microscopy for high-speed, *in vivo* cellular imaging," Opt. Lett. **28**, 2064-2066 (2003).
18. M. R. Hee, D. Huang, E. A. Swanson and J. G. Fujimoto, "Polarization-sensitive low-coherence reflectometer for birefringence characterization and ranging," J. Opt. Soc. Am. B **9**, 903-908 (1992).
19. I. Freund, M. Deutsch and A. Sprecher, "Connective tissue polarity: optical second-harmonic micrscopy, crossed-beam summation, and small-angle scattering in rat-tail tendon," Biophys. J. **50**, 693-712 (1986).
20. Y. Uesu and N. Kato, "Multi-purpose nonlinear optical microscope. Its principles and applications to polar thin-film observation," Phys. Solid State **41**, 688-692 (1999).
21. C. Vinegoni, J. S. Bredfeldt, D. L. Marks and S. A. Boppart, "Nonlinear optical contrast enhancement for optical coherence tomography," Opt. Express **12**, 331-341 (2004).
http://www.opticsexpress.org/abstract.cfm?URI=OPEX-12-2-331
22. E. Beaurepaire, L. Moreaux, F. Amblard and J. Mertz, "Combined scanning optical coherence and two-photon-excited fluorescence microscopy," Opt. Lett. **24**, 969-971 (1999).
23. J. P. Dunkers, M. T. Cicerone and N. R. Washburn, "Collinear optical coherence and confocal fluorescence microscopies for tissue engineering," Opt. Express **11**, 3074-3079 (2002).
http://www.opticsexpress.org/abstract.cfm?URI=OPEX-11-23-3074

1. Introduction

Optical second harmonic generation (SHG) arises from the interaction of large electric fields with a medium with nonlinear polarizability at the molecular level. The incident electric field E induces a polarization P in the sample given by

$$P = \varepsilon_0 \left(\chi^{(1)} E + \chi^{(2)} E E^* + \ldots \right) \qquad (1)$$

where $\chi^{(n)}$ represents the nth-order susceptibility tensor. The second term in Eq. (1) in turn results in a coherent output electric field at twice the frequency of the incident wave, and quadratically dependent upon the incident electric field amplitude. The second-order nonlinear susceptibility $\chi^{(2)}$ vanishes in centrosymmetric media. Thus, SHG provides intrinsic molecular contrast, sensitive to surfaces or macromolecules lacking inversion symmetry. SHG is a powerful technique in surface chemistry studies, with applications including measurements of surface properties of monolayers, molecular orientation of adsorbates, and interfacial reaction kinetics [1,2]. In biological applications, SHG has recently emerged as a valuable tool for imaging cell membranes and structural proteins such as collagen, myosin, and microtubules, without the need for exogenous contrast agents or genetically modified species [3-7].

Since SHG is a coherent optical interaction, the SHG field generated in the sample has a deterministic phase relationship with the incident electric field. It is therefore possible to detect SHG interferometrically, by mixing the SHG field from a sample of interest with that of a reference, typically a crystal with large $\chi^{(2)}$. Interferometric SHG (ISHG) was originally introduced in 1965 [8] to measure the complex $\chi^{(2)}$ coefficients for various semiconductor materials. Phase-sensitive measurements of surface SHG has since been implemented for background suppression of bulk SHG, characterization of molecular orientation of thin films, and measurement of laser coherence [9,10]. Displacing the frequency of the reference beam, by amplitude or phase modulation, allows heterodyne detection for improving signal-to-noise ratio and detecting weak signals. In a recent study, heterodyne detection enabled a surface SHG sensitivity of 6 photons/s [11]. The utility of heterodyne detection in biomedical optics is exemplified by optical coherence tomography (OCT) [12], whereby interferometric

detection has been successfully used to perform high resolution, cross-sectional imaging of living tissues.

To our knowledge, heterodyne detection has yet to be demonstrated for SHG microscopy. Due to the high peak intensities of the optical fields necessary to generate a detectable signal, nonlinear optical imaging in scattering media is typically limited to a few hundred micrometers beneath the surface [13]. It would be advantageous to further extend the penetration depth of SHG for *in vivo* deep tissue imaging. Here we demonstrate a novel SHG microscope that employs heterodyne detection of the second harmonic fields between a sample and reference crystal. Additionally, this microscope incorporates the imaging capability of optical coherence microscopy (OCM) [14] for simultaneous coherent imaging of linear and nonlinear scattering. OCM is an extension of OCT using high numerical aperture optics and transverse scanning to generate high resolution *en face* images of sample reflectance and improve rejection of light outside the focal volume.

2. Methods

A schematic of the interferometric second harmonic generation (ISHG) microscope is shown in Fig. 1. Sub-100 fs pulses from a mode-locked Ti:sapphire laser (center wavelength $\lambda = 800$ nm, bandwidth $\Delta\lambda \sim 10$ nm) are incident on a modified Michelson interferometer. At the first beamsplitter (BS1) half of the light is directed to the microscope and the other half is directed to a reference mirror mounted on a piezoelectric transducer. The reference arm is scanned at 100 Hz over 5 µm to generate heterodyne frequencies of 2.5 kHz and 5 kHz at the fundamental and second harmonic wavelengths, respectively. A portion of the light returning from the reference mirror is directed by BS2 to a 1.5 mm thick lithium triborate (LBO) crystal, in which the reference SHG signal is generated by type I phase-matching ($\theta = 90°$, $\phi \sim 30°$). A half-wave plate inserted before the crystal controls the SHG efficiency, resulting in a variable reference arm power for optimizing signal-to-noise ratio [15,16]. Residual power at the fundamental wavelength is removed using a 2.8 mm thick Schott BG39 filter and directed towards the detectors.

In the sample arm, the incident beam is focused by a high-NA objective lens (20X, 0.75 NA) resulting in a diffraction-limited point spread function radial dimension (full width at
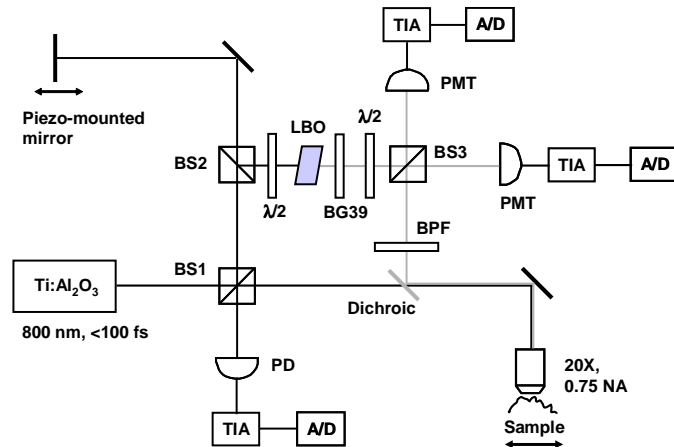

Fig. 1. Schematic of interferometric second harmonic generation (SHG) microscope. The fundamental wavelength is shown in black and the second harmonic is shown in gray. BS1-BS3, 50/50 beam splitters; $\lambda/2$, half-wave plate; PD, photodiode; PMT, photo-multiplier tube; LBO, lithium triborate crystal; GRIN, graded-index collimating lens; BPF, bandpass filter; NA, numerical aperture; TIA, transimpedance amplifier, A/D, analog-to-digital conversion.

half maximum) of ~1.4 μm on the sample. (For some of the experiments, the objective lens was underfilled, resulting in a radial dimension of ~3.5 μm.) Light at the fundamental wavelength reflected from the sample and reference interferes at a silicon photodiode, resulting in a conventional OCM signal. No confocal pinhole was used in front of the detector. The backreflected SHG beam in the sample path is separated from the fundamental using a dichroic filter and combined with the reference SHG at BS3. Residual light resulting from sample reflectance or two-photon excited autofluorescence is removed using a 30-nm bandwidth bandpass filter centered at 400 nm. The signal in the ISHG channel is detected using a photomultiplier tube with reduced gain for analog operation. Both beams emerging from BS3 are collected for dual balanced detection, used to increase the collection efficiency of the SHG signal and to eliminate common-mode noise such as source amplitude fluctuations. The OCM and ISHG channels are simultaneously digitized at 5-10 times the Nyquist frequency using a 16-bit analog-to-digital converter (A/D). An image is formed at each detector by scanning the sample under the probe beam using a precision computer-driven mechanical translation stage. Currently the image acquisition time of ~27 min for a 128×128 pixel image is limited by the scan rate of the reference piezo and the acquisition rate of the A/D, although real-time imaging at several frames per second is feasible with rapid scanning reference delay lines [17].

The interferometric component of the detector current in each channel ($n = 1, 2$) is given by

$$i_{dn} \propto E_{rn} E_{sn} \cos(2k_n \delta l) \qquad (2)$$

where E_{rn} and E_{sn} represent the electric fields from the reference and sample arms, respectively, that are incident on the detector for either the OCM ($n = 1$) or the ISHG ($n = 2$) channel; k_n is the corresponding wavenumber in each channel; and δl is the axial position of the reference arm. Due to the nonlinear nature of the ISHG signal, the field amplitudes in Eq. (2) for $n = 2$ are in turn proportional to the square of the incident field amplitude E_0. To first order, the detector current in the ISHG channel is described by

$$i_d \propto \beta \chi_r^{(2)} \chi_s^{(2)} I_0^2 \cos(2k_2 \delta l) \qquad (3)$$

where $\chi_r^{(2)}$ and $\chi_s^{(2)}$ are the active nonlinear susceptibility coefficients of the reference and sample materials, respectively, $I_0 = |E_0|^2$ and β is an efficiency factor accounting for the mode overlap and polarization mismatch of the reference and sample beams, detector responsivity, and losses in the optical system due to the interferometer topology. In practice, an empirical expression for the detector current must account for the spatiotemporal behavior of the incident wave and the nonlinear interaction length in the medium. The purpose of Eq. (3) is to illustrate the quadratic dependence of the signal on the source power, the scalar contribution of the reference arm (often termed "heterodyne gain",) and the modulation of the photodetector output by scanning the reference mirror.

3. Results

Interference patterns as a function of reference arm position are shown in Fig. 2 for both the OCM and SHG channels. The sample was a 1 mm thick β-barium borate (BBO) crystal oriented for type I phase matching. The axial point spread function [12] is given by the confocal parameter of the beam and the width of the interference patterns, which is determined by the coherence length of the source, $l_c = (2\ln 2)\lambda^2 / \Delta\lambda$, and by dispersion mismatch in the sample and reference arms. The optimal spatial resolution results when dispersion in the two arms is equal. The theoretical widths of the coherence functions are 28

µm and 19 µm for the OCM and ISHG channels, respectively. The corresponding measured values were 32 µm and 36 µm. The large discrepancy of coherence gate in the ISHG channel is due to dispersion mismatch between the reference and sample paths, and can be corrected by inserting appropriate dispersion compensating prisms in one of the paths. To obtain Fig. 2, the reference arm was scanned a large enough distance to recover the entire interferogram, while the sample was held in the objective focal plane to maintain a stationary confocal gate. For use in microscopy, the reference arm is scanned 5 µm instead, in order to minimize the detection volume. At this scale (Fig. 3) the individual fringes can be identified, indicating that the ISHG fringe spacing is half that of the OCM channel.
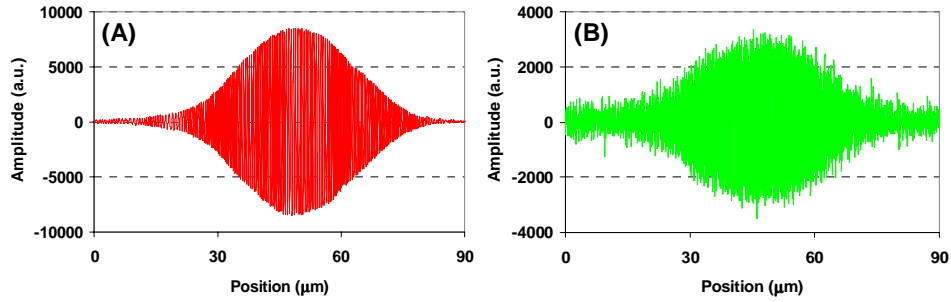
Fig. 2. Interferometric detector output as a function of reference arm position for the (a) OCM and (b) SHG channels, using a 1 mm thick BBO crystal as the sample.
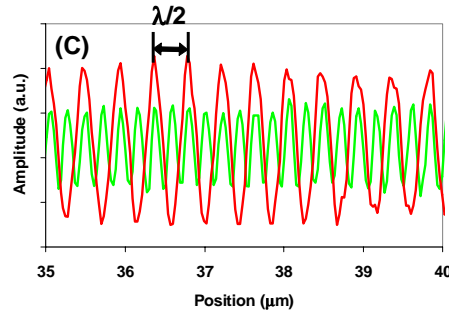
Fig. 3. Detail of interferometric detector outputs indicates a fringe spacing of 400 nm for the OCM channel and 200 nm for the ISHG channel.

In order to verify the simple model for the photodetector output [Eq. (3)], the peak amplitude of the interferogram is shown in Fig. 4(a) to scale quadratically with the source power, with a fitted slope of 2.08. Similar data for the OCM channel scaled linearly with source power (not shown.) As given by Eq. (2), it is expected that the photodetector output also scales linearly with the electric field contributed from the reference arm. Since the reference LBO crystal is oriented for type I phase matching, rotating the polarization state of the light controls the reference arm conversion efficiency without altering the polarization state incident on the detector. The ISHG peak amplitude is plotted as a function of the waveplate angle ψ (Fig. 4(b)) for a half-wave plate placed prior to the reference crystal. The waveplate rotates the beam by 2ψ, and only the component polarized along the phase matched axis of the reference LBO crystal, which scales with $\cos(2\psi)$, is converted to the second harmonic frequency. Therefore, a $\cos^2(2\psi)$ fit indicates the linear dependence of the ISHG signal on the electric field emerging from the reference arm. The relative contribution of the reference arm to the signal can be set to optimize the signal-to-noise ratio [16].
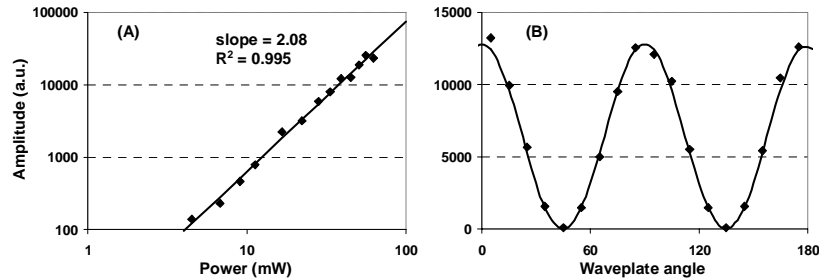
Fig. 4. (a) Peak ISHG amplitude as a function of power incident on the sample, indicating the quadratic nature of the nonlinear process. The OCM signal amplitude scaled linearly with incident power (not shown.) (b) Variation of ISHG signal as a function of the entrance waveplate angle ψ, and $\cos^2(2\psi)$ fit.

Simultaneous OCM and ISHG microscopy images were obtained of BBO microcrystals ranging from 1-50 μm in size (Fig. 5.) The total image sampling volume was $100 \times 100 \times 5$ μm^3. The OCM channel measures sample reflectance that is coherent with the reference arm, whereas the ISHG channel selects only the coherent second harmonic signal. At each lateral position in each image, the pixel intensity is obtained from the average amplitude of the 5 μm axial interference pattern, demodulated at the heterodyne frequency of the corresponding channel. Phase sensitive demodulation (or Hilbert transformation) of the photodetector output provides both the amplitude and phase of the sample SHG. The axial sectioning capability of the microscope was demonstrated by obtaining images at two different depths, separated by approximately 30 μm. Note that the ISHG axial resolution is determined by the quadratic dependence of the microscope objective point spread function at ~4 μm.

Polarization sensitive detection, illustrated in Fig. 6, was achieved by controlling the output polarization state of the reference SHG field with a half-wave plate. Images were
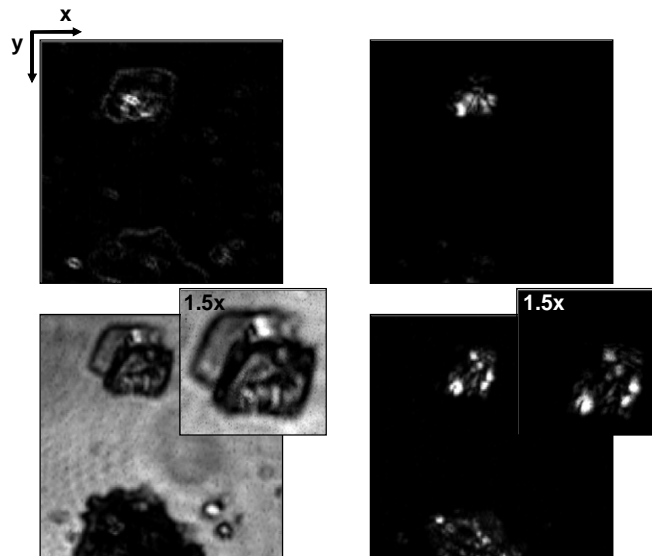

Fig. 5. Simultaneous OCM (left) and ISHG (right) images from BBO microcrystals at two different depths. The image area is 100×100 μm^2, containing 128×128 pixels. The signal at each pixel is the average amplitude over a 5μm depth. Inset: 40×40 μm^2 image of a single microcrystal fragment shows greater detail. The bright background in the bottom OCM image resulted from focusing near the glass slide.

obtained for the polarization state parallel and perpendicular to the incident wave. The signal amplitude in the two orthogonal channels varies across the crystals, indicating microstructural variations in orientation. A single lateral scan is also shown, revealing further detail, including regions with high extinction in one of the orthogonal polarization states. True polarization diversity detection can be achieved by replacing the final cube beamsplitter, BS3 (cf. Fig. 1) with a polarizing beam splitter, and setting the reference arm polarization at 45° [18]. In principle, modulation of the incident polarization state in the sample arm, along with polarization sensitive detection, can be used to map the complex nonlinear susceptibility coefficients of the sample.
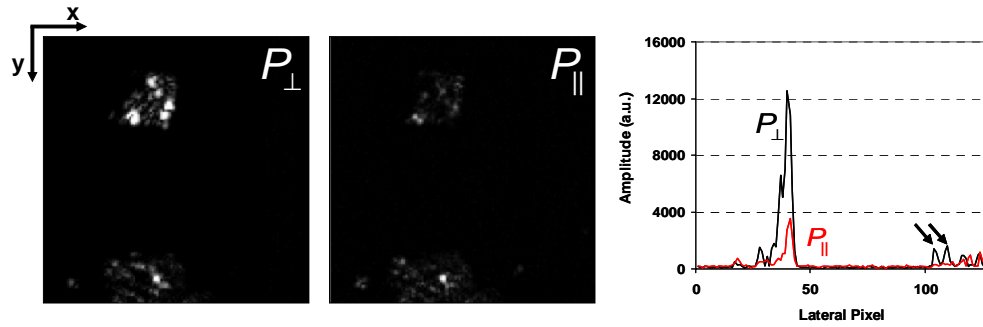

Fig. 6. Polarization sensitive detection in ISHG microscopy. The polarization state of the reference arm was held perpendicular ($\perp$) and parallel ($\parallel$) to the incident wave. A single lateral scan through both images reveals structural detail of the crystals and may potentially be used for mapping the complex nonlinear susceptibility of the sample. Arrows indicate a region polarized along one of the axes, with high extinction in the orthogonal axis.

4. Conclusions

Interferometric detection of SHG has previously been used to improve the sensitivity of SHG and to measure the complex nonlinear susceptibility of surfaces [10,11]. ISHG microscopy was suggested, to our knowledge, as early as 1986 [19], and demonstrated for imaging ferroelectric thin films [20]. Here we have demonstrated a novel microscope based on heterodyne detection of SHG from a sample and reference. Heterodyne detection may be implemented to probe any coherent interaction, including higher order harmonic interactions and coherent anti-Stokes Raman scattering, as demonstrated recently [21]. Heterodyne detection may potentially be used to extend the penetration depth of SHG in scattering media such as biological tissue. Propagation of light through highly scattering media results in a randomization of electric field polarization and degradation of the mode quality, potentially leading to a degradation of coherence, and hence, net heterodyne efficiency. Coherent detection thus enhances the rejection of background scattered light that has reduced coherence with the reference field. The effect of scattering on direct versus interferometric detection remains to be explored. Our instrument simultaneously performs reflectance imaging with OCM. The instrument may be modified to a multimodal microscope, combining ISHG, OCM, and multiphoton fluorescence microscopy, by placing the appropriate filters after the final cube beamsplitter. Combined OCM and fluorescence microscopes have been previously demonstrated for various applications in biology and tissue engineering [22,23].